



## City Research Online

### City, University of London Institutional Repository

---

**Citation:** Chassaing, J. C., Sayma, A. I. & Imregun, M. (2008). A combined time and frequency domain approach for acoustic resonance prediction. *Journal of Sound and Vibration*, 311(3-5), pp. 1100-1113. doi: 10.1016/j.jsv.2007.10.006

This is the accepted version of the paper.

This version of the publication may differ from the final published version.

---

**Permanent repository link:** <https://openaccess.city.ac.uk/id/eprint/7905/>

**Link to published version:** <https://doi.org/10.1016/j.jsv.2007.10.006>

**Copyright:** City Research Online aims to make research outputs of City, University of London available to a wider audience. Copyright and Moral Rights remain with the author(s) and/or copyright holders. URLs from City Research Online may be freely distributed and linked to.

**Reuse:** Copies of full items can be used for personal research or study, educational, or not-for-profit purposes without prior permission or charge. Provided that the authors, title and full bibliographic details are credited, a hyperlink and/or URL is given for the original metadata page and the content is not changed in any way.

---

---

---

City Research Online:

<http://openaccess.city.ac.uk/>

[publications@city.ac.uk](mailto:publications@city.ac.uk)

---

# A Combined Time and Frequency Domain Approach for Acoustic Resonance Prediction

J.C. Chassaing\*, A. I. Sayma, M. Imregun

<sup>a</sup>*Université Pierre et Marie Curie, Institut Jean Le Rond d'Alembert, case 161, 4 place Jussieu, 75252 Paris, F*

<sup>b</sup>*Imperial College London, Department of Mechanical Engineering, South Kensington Campus, London SW7 2AZ, UK*

---

## Abstract

A general time and frequency methodology has been developed to identify acoustic resonance conditions of internal flow configurations. The resonant frequencies and the corresponding acoustic modes are determined by imposing onto the flow a time-dependent excitation at several locations on the boundary. The resulting time-domain responses of the pressure signals, which are computed via an unsteady Favre-Reynolds averaged Navier-Stokes solver, are used to determine the frequency response function matrix of the fluid which can be considered to be a multiple-input multiple-output system. The main test case was selected to be a closed-end cylindrical duct for which the effect of different excitation techniques on the predicted resonant acoustic field is discussed in detail. The last test case deals with the acoustic characterization of a 2-D channel with symmetric bumps and an inlet flow velocity of  $17 \text{ ms}^{-1}$ . It is shown that the methodology was suitable for identifying both axial and transverse acoustic modes in a 10 Hz - 3 kHz frequency range.

---

## 1 Introduction

In many aerospace applications, aeroacoustic resonance of internal flow configurations is considered to be an extremely undesirable phenomenon which must be avoided during the design process. The excitation of the acoustic modes in core volumes, such as the combustion chamber of liquid-propellant[1, 2] or

---

\* Corresponding author.

*Email addresses:* [jean-camille.chassaing@upmc.fr](mailto:jean-camille.chassaing@upmc.fr) (J.C. Chassaing), [a.sayma@imperial.ac.uk](mailto:a.sayma@imperial.ac.uk) (A. I. Sayma), [m.imregun@imperial.ac.uk](mailto:m.imregun@imperial.ac.uk) (M. Imregun).

solid-propellant[3–5] rocket motors, can lead to uncontrolled self-sustained instabilities. Similarly, under critical conditions, rotors of high-pressure turbo-compressors can exhibit high vibration levels due to wake-excited acoustic resonances[6]. Acoustic/flow coupling can also play a crucial role on performance degradations and extra tone noise levels of configurations such as shock wave/ boundary layer interactions[7], convergent-divergent nozzles at off-design conditions[8] or open-cavities flow resonance[9].

Due to the difficulties of predicting acoustic resonance using analytical or numerical methods, much of the work has been conducted experimentally, similar to the shaker excitations used for modal extraction in structural engineering. A classical approach to establish possible links between observed instabilities and acoustic resonances is based on white-noise excitation of the component under study and the filtering of acoustic resonance frequencies by using loudspeakers[10–14]. In many cases, such experimental simple acoustic characterization may well provide crucial information about flow-induced resonant sound generation during operating conditions[15, 16].

Due to significant improvements in computational fluid dynamics methods, turbulence modeling and computing hardware, unsteady Reynolds-averaged Navier-Stokes (RANS) equations can, in principle, be used for time-domain investigations of acoustic resonance phenomena. However, neither the application of a suitable excitation to identify the acoustic resonances without altering the nature of the flow, nor the interpretation of the results is straightforward. This paper aims at developing a general time-domain RANS methodology to identify acoustic resonances of core volumes commonly encountered in engineering applications.

## 2 Basic methodology

The dynamic behavior of a multiple input multiple output (MIMO) linear system can be described through the following frequency-domain relationship

$$\mathbf{H}_{xy}(f) = \mathbf{G}_{xx}^{-1}(f)\mathbf{G}_{xy}(f) \quad (1)$$

where  $\mathbf{H}_{xy} \in \mathbb{C}^{N_i \times N_o}$  is the complex-valued matrix of frequency response functions (FRF matrix) between the  $N_i$  inputs and the  $N_o$  outputs of the system,  $\mathbf{G}_{xx} \in \mathbb{R}^{N_i \times N_i}$  is the real-valued squared matrix of the  $N_i \times N_i$  one-sided auto-spectral density of the inputs, and  $\mathbf{G}_{xy} \in \mathbb{C}^{N_i \times N_o}$  is the complex-valued rectangular matrix of the  $N_i \times N_o$  cross-spectral density between the  $N_i$  inputs and the  $N_o$  outputs. The auto- and cross- spectral density matrices are determined by

$$\mathbf{G}_{xx}(f) = 2 \lim_{T \rightarrow \infty} \frac{1}{T} E [\mathbf{X}^*(f) \mathbf{X}^T(f)] \quad (2)$$

$$\mathbf{G}_{xy}(f) = 2 \lim_{T \rightarrow \infty} \frac{1}{T} E [\mathbf{X}^*(f) \mathbf{Y}^T(f)] \quad (3)$$

where  $E$  denotes the expectation operator and  $\mathbf{X} = [X_1, X_2, \dots, X_{N_i}]^T$  and  $\mathbf{Y} = [Y_1, Y_2, \dots, Y_{N_o}]^T$  are two vectors representing the Fourier transform of the  $N_i$  inputs and the  $N_o$  outputs respectively. The inverse of the auto-correlation matrix  $\mathbf{G}_{xx}^{-1}$  is computed using singular value decomposition. From a practical point of view, the record time is finite since the numerical simulation with the RANS code is for a finite duration. Consequently, equation (1) gives only an approximation to the FRF matrix.

In the present work, the inputs correspond to time-dependant excitations which are applied at several boundary locations to the flow. The response is computed at several locations inside the core volume solving the Favre-Reynolds-averaged Navier-Stokes equations. Such time-domain information allows the construction of a frequency response function of the core volume from which both the acoustic resonances and associated mode shapes are determined.

### 3 Test-case 1: 1-DOF mechanical system

The previous methodology is validated by comparison with the exact transfer function of a single input single output configuration. A viscously damped 1-DOF mechanical system is excited by a stationary random forcing function and the corresponding time-domain equation of motion are

$$m\ddot{y}(t) + c\dot{y}(t) + ky(t) = x(t) \quad (4)$$

where  $m = 17.5$  kg is the mass of the system,  $c = 350$  N.s.m<sup>-1</sup> denotes the viscous damping coefficient,  $k = 1.7 \times 10^4$  kN.m<sup>-1</sup> is the stiffness coefficient,  $x(t)$  and  $y(t)$  are respectively the input random force and the resulting output displacement. A 4-step Runge-Kutta finite difference scheme is used to compute the time domain response of the system used to identify the frequency response function. The random behavior of the input force  $x(t)$  is prescribed within a range of  $\pm 4.5$  N and a different value of the input signal is imposed at each time step  $\Delta t = 10^{-4}$  s. Results are compared with the exact solution of the frequency response function defined by

$$|H_{xy}(f)| = \left\{ k \sqrt{[1 - (f/f_n)^2]^2 + [2\xi f/f_n]^2} \right\}^{-1} \quad (5)$$

where  $\xi = c/(2\sqrt{km})$  denotes the damping factor and  $f_n = 1/(2\pi)\sqrt{(k/m)}$  represents the undamped natural frequency.

A comparison of the gain factor between the analytical solution and two numerical results is given in Figure (1). The first numerical result is obtained using only one sample record ( $N_k = 1$ ) and the frequency response function is determined from the auto- and cross-spectrum one-sided density functions  $G_{xx}$  and  $G_{xy}$  (equations 2 and 3). The Fourier transforms of the input and output signal are computed over a single record time of length  $T = 0.2047$  s corresponding to  $n_{\max} = 2048$  iterations. This procedure is sufficient to give a good estimation of the resonance frequency as shown by the position of the peak in the gain factor distribution (Figure 1) where the exact solution and the computed resonance frequencies are respectively  $f_r^{\text{exact}} = 158.34$  Hz and  $f_r^{\text{comp.}} = 162.9$  Hz, according to a frequency resolution of  $\Delta f = 4.88$  Hz. However, these predictions become unacceptable for very high frequencies, introducing substantial spurious noise. A second computational test was performed defining the total computational time  $T_{\max} = N_k T$  based on a multiple of the previous record length  $T$  and on the total number of the sample records  $N_k$ .

In the case of the results presented in Figure (1), the number of sample records is  $N_k = 25$  and the length of each sample record remains unchanged ( $T = 0.2047$  s and  $n_{\max} = 2048$ ). The main effect of averaging over several sample signals when computing the frequency response function results in a substantial smoothing of the numerical solution. It can be observed that the computed value of the resonance frequency with  $N_k = 25$  ( $f_r = 157.4$  Hz) is closer to the exact solution of  $f_r^{\text{exact}} = 158.34$  Hz as compared with  $f_r = 162.9$  Hz for  $N_k = 1$ . Furthermore, the shape of the gain factor distribution is corrected when the frequency increases, giving a mean slope after the peak which can be superposed to the slope of the exact solution. Similar improvements were obtained on the phase factor prediction where the phase shift near the resonance frequency was in satisfactory agreement with the exact solution.

#### 4 Test-case 2: Acoustic resonance in a closed-end tube

The purpose of the second test case is to re-visit the experimental work of Anthoine *et al.*[10] on the zero-flow acoustic characterization of a typical solid propellant booster. This axisymmetric test facility consists of a contoured nozzle with a throat diameter of 30 mm, a section diameter of 76 mm and a booster length ( $L = 405$  mm). In order to get a better understanding of the flow-acoustic coupling mechanisms in such configuration, Anthoine *et al.*[10] began their experimental investigations by a preliminary study where a loud-speaker is placed at the throat of the nozzle whereas the original porous wall

at the right end is replaced by a solid wall so that the duct has closed ends. The experimentally-determined frequencies of the first two axial acoustical modes were found to be relatively close to the analytically-determined resonance frequencies of a close-ends circular cylinder.

Consequently, it was assumed in this work, that the acoustic characterization of booster could be approximated by a cylinder of diameter 76 mm without loss of generalities. An unstructured mesh was generated using 31 circumferential nodes, each duct end surface was discretized with triangular elements and 56 nodes were used along the length of the cylinder with quadrilateral elements (Figure 2).

The main difficulty was the formulation of a suitable unsteady excitation mechanism similar to white-noise that would be provided by a loudspeaker. After many attempts, it was found that best results were obtained when the left end surface of the duct was modeled with an elastic membrane subject to random deformations of the form

$$x_{i,j,k}(t) = x_{i,j,k}^0 + \chi_{i,j,k}(t) \cos [2\pi f_{\text{ex}}(t) t] \quad \forall (i, j, k) \in \partial S \quad (6)$$

where  $\partial S$  denotes the surface of the vibrating wall,  $x_{i,j,k}$  is the instantaneous position of the wall at node  $(i, j, k)$ ,  $x_{i,j,k}^0$  determines the unperturbed position of the membrane,  $\chi_{i,j,k}$  is the maximum vibration amplitude at each instant, and  $f_{\text{ex}}$  denotes the excitation frequency of the forced displacement of the membrane. These conditions correspond to a non-uniform imposed displacement of the membrane  $x_{i,j,k}(t)$  with a random amplitude  $\chi_{i,j,k}$  at each time step. The excitation frequencies  $f_{\text{ex}}$  are prescribed using a time-dependent formulation corresponding to a linear variation over a user-defined bandwidth of interest

$$f_{\text{ex}}(t) = f_{\text{low}} + (f_{\text{high}} - f_{\text{low}}) \frac{t}{t_{\text{max}}} \quad (7)$$

where  $f_{\text{low}}$  and  $f_{\text{high}}$  are the lower and the upper values of the excitation window and  $t_{\text{max}} = n_{\text{max}} \Delta t$  is the total simulation time. The duct was excited at a single axial position ( $x/L = 0$ ), while the response was computed at 13 equally spaced points along the duct in order to be able to identify the mode shapes. The variation of the applied excitation frequency against time was defined as  $[f_{\text{low}}; f_{\text{high}}] = [100 \text{ Hz}; 1 \text{ kHz}]$ . The maximum amplitude of the membrane displacement was chosen such that the corresponding pressure perturbation was 0.5 % of the unperturbed pressure. The corresponding frequency increment is  $(\Delta f)_{\text{ex}} = (n_{\text{max}} \Delta t)^{-1} = 8.13 \text{ Hz}$ , the total number of time instants being  $n_{\text{max}} = 8196$  and the time step  $\Delta t = 1.5 \times 10^{-5} \text{ s}$ . A 3-D finite-volume Favre-Reynolds averaged Navier-Stokes solver, based on an  $O(\Delta x^2)$  centered scheme [17] was used to implement the excitation boundary condition. The size of the time step was chosen to have 66 points per period in order to ensure

the correct time discretization of the signal at the highest excitation frequency  $f_{\text{high}} = 1$  kHz.

The time history of the axial velocity at  $x = 0$  (Figure 3) exhibits the expected random behavior of the excitation signal whereas the flow response at  $x = L/2$  (Figure 4) clearly shows two vibration modes at two distinct instants ( $t_1 \cong 5.5 \times 10^{-2}$  s,  $t_2 \cong 1.05 \times 10^{-2}$  s), corresponding approximately to 450 Hz and 800 Hz. Both the pressure and velocity signals were stored at each time step and the spectra at each output point were computed by averaging the Fourier transforms of each output  $n_o \in [1, N_o]$

$$\bar{X}_u(f) = \frac{1}{N_o} \sum_{n_o=1}^{N_o} \left[ \int_0^T u_{n_o}(t) e^{-i2\pi ft} dt \right] \quad (8)$$

where  $u_{n_o}$  is the instantaneous velocity at output  $n_o$  and  $\bar{X}_u$  the averaged velocity spectrum over the  $N_o$  outputs. A typical velocity spectrum is presented in Figure (5). The two distinct peaks lead to the identification of the acoustic resonant conditions.

The present methodology was applied to 3 different duct lengths ( $L = 231$  mm,  $L = 292.5$  mm,  $L = 405.5$  mm) and compared with analytically-derived resonance frequencies values  $f_n^{\text{exact}} = n \frac{a}{2L}$  for a closed circular cylinder, where  $a$  is the speed of sound and  $n$  denotes the mode number. The discrepancies between the computed and the analytical results are below the frequency resolution ( $\Delta f = 8.13$  Hz) for both first two axial modes except for the shorter booster length  $L = 231$  mm ( $f^{\text{comp.}} = 710$  Hz and  $f^{\text{exact}} = 742$  Hz). The axial mode shapes were determined by considering the peak value of each output spectrum at the two acoustic frequencies. As it can be seen from Figure (6), the computed non-dimensional pressure mode shape is in good agreement with the exact solution  $\Phi^n(x) = \cos(n\pi x/L)$ . The wavelength of the first acoustic mode is twice the length of the cylinder and the wavelength of the second acoustic mode is equal to the length of the cylinder. Furthermore, as predicted by theory, an inspection of Figures (6) and (7) reveals that there is a phase shift of a quarter wavelength between the pressure and velocity mode shapes.

### *Influence of the frequency excitation range*

In addition to the previous results, the velocity spectrum  $\bar{X}_u$  was computed for three different excitation cases: (a) [50 Hz – 999 Hz]; (b) [100 Hz – 600 Hz]; and (c) [300 Hz – 900 Hz]. All computations were performed with  $\Delta t = 1.5 \times 10^5$  s and  $n_{\text{max}} = 8192$ . The results are presented in Figure (8) and the effect of the excitation range on the predicted frequencies is self evident. Case (b) captures

the first axial mode only ( $f^{1A} = 420$  Hz) since the second mode is outside the range. Case (c), the excitation window of which has been extended (Figure 8), is seen to capture both modes ( $f^{1A} = 420$  Hz and  $f^{2A} = 840$  Hz). Case (a), which uses a broad bandwidth, also captures both modes but the peak amplitudes are seen to be different. When the excitation range is below 200 Hz, there is no flow response when the excitation window is located apart from significant frequencies (Figure 8, case (c),  $f < 200$  Hz). Otherwise there is a flow response for  $f_{\text{ex}} < 200$  Hz when the excitation window corresponds to the frequency domain of interest. This relatively small but not negligible amplification represents approximately 8 % of the first mode peak amplitude and may be assimilated to the level of the residual noise introduced by the solver.

### *Effect of the time step*

Two numerical simulations, corresponding to time steps of  $\Delta t = 1.5 \times 10^{-5}$  s and  $\Delta t = 8 \times 10^{-6}$  s, were conducted on a cylinder with a length of  $L = 231$  mm. The time record lengths were  $n_{\text{max}} = 8192$  and  $n_{\text{max}} = 16384$  respectively. The corresponding computed pressure spectrum amplitudes are plotted in Figure (9). Both computations were able to capture the resonant frequency of the first longitudinal mode, the value of which agrees with the analytical solution ( $f_{\text{exact}}^{1A} = 742$  Hz). However, it is immediately seen that the shorter time step, with 168 points per period, yields a much clearer spectrum than the longer time step which only has 90 time steps per period. The second axial mode ( $f_{\text{exact}}^{2A} = 1485$  Hz) was not captured by the numerical simulations because the excitation frequency window was selected to capture the first mode only.

### *Influence of the excitation mechanism*

Finally, cylinder dimensions of  $L = 1$  m and  $D = 0.5$  m were selected in order to investigate the influence of membrane behaviour on the flow excitation. The discretization of the cylinder geometry resulted in 31 equally-spaced circumferential nodes and 49 axial nodes, the total number of grid points being 4998. A time step of  $\Delta t = 1.5 \times 10^{-5}$  s and an excitation window of [10 Hz; 999 Hz] were used. The maximum amplitude of the vibrating membrane corresponds to a 1 % variation of the steady pressure inside the cylinder. Additional numerical parameters are  $n_{\text{max}} = 4096$ ,  $T = 6.1 \times 10^{-2}$  s and  $\Delta f = 8.13$  Hz. Two sets of calculations, corresponding to elastic and rigid membranes respectively, were considered. The rigid membrane calculation was performed by setting the axial displacement of the membrane, denoted by  $\chi$  in (equation

6), to a constant value, independent of grid position. The results are plotted in Figure (10) which clearly shows that the use of an elastic membrane is a much better way of exciting the flow. Although the rigid membrane is able to capture the first two modes, it also introduces spurious oscillations which hinder the identification of the third and fourth modes in Figure (10). The first three mode shapes obtained from the elastic membrane calculation are plotted in Figure (11). The time step corresponds to 392 time points per period used to describe the fundamental acoustic mode ( $f^{1A} = 1700$  Hz). Although the mode shapes are captured with good accuracy, a small deformation occurs near the membrane at  $x = 0$  because the grid points at that location are moving with the mesh to provide the membrane flexibility.

### 5 Test-case 3: Acoustic characterization of the Délerly B nozzle

Here, the aim is to demonstrate the capability of the method to deal with practical flows. 2-D RANS computations were performed on the Délerly B symmetric bump channel with an adjustable second throat[18]. This nozzle has a length of  $L = 629$  mm and a height of  $H = 100$  mm. The minimum sections at the first and second throats are located at  $x_{T_1} = 90$  mm and  $x_{T_2} = 550$  mm respectively (Fig. 12, 13). Both steady and unsteady flows were computed using a multi-block structured Favre-Reynolds-averaged Navier-Stokes solver with  $O(\Delta x^3)$  upwind-biased van Leer-flux-vector-splitting scheme and moving grid capabilities[19]. The computational mesh is based on  $201 \times 101$  grid points in the streamwise ( $x$ ) and wall-normal ( $y$ ) directions respectively (Fig. 12) and the minimum non-dimensional grid spacing at the wall is  $y_w^+ = 0.5$ . The inlet flow velocity is  $u_0 = 17$  ms<sup>-1</sup>. In this study, the excitation mechanism was chosen to be generated by rigid and elastic vertical displacements of the upper wall corresponding to the convergent-divergent parts of the 2nd throat ( $x \in [550 \text{ mm}, 629 \text{ mm}]$ ). An array of  $14 \times 7$  ( $x$ -wise  $\times$   $y$ -wise) "pressure sensors" was used to compute the FRF matrix (Fig. 13). The time-step was set to  $\Delta t = 7 \times 10^{-6}$  s and the total computational time  $T = 0.11$  s corresponds to a frequency resolution  $\Delta f = 8$  Hz.

A preliminary study was conducted on the unsteady flow response resulting from two different deformations of the 2nd throat. Figure (14) presents a comparison of the pressure amplitude spectra at probe  $x = 350$  mm and  $y = 30$  mm resulting from random displacements of the 2nd throat and from sine sweep oscillations. As expected both approaches give the same acoustic resonance frequencies, but it appears that the white noise excitation yields noisier pressure spectra than when using a sine sweep excitation (Fig. (14)). Therefore, further studies will be performed by imposing a sine oscillation to the 2nd throat (Fig. 15).

It can be seen from Figure (16) that the pressure time history of the flow response, picked up at the reference probe, exhibits a high response level at selected frequencies. This is confirmed by the amplitude and phase plots of the pressure spectrum (Fig. 17). It must be noted that these spectra, which are computed without the use of FRF windowing or sample averaging procedures, are completely free from spurious noise.

The resonance conditions, which are characterized by peaks in the pressure spectrum amplitude, are clearly visible up to 3000 Hz (Fig. 17). As expected, the first resonance frequency ( $f_1 = 237$  Hz) matches closely the axial acoustic modes analytically computed assuming zero mean-flow ( $f_{\text{exact}}^{1A} = 239$  Hz). The Strouhal number, based on the bump length  $\chi$  is  $Sr = f^{1A}\chi/u_0 = 2.8$  for the first acoustic mode. It is interesting to note that the pressure spectrum shows, in a frequency range of 1700 Hz up to 2100 Hz, two peaks whose frequencies ( $f_8 = 1731$  Hz and  $f_9 = 1845$  Hz) do not correspond to a multiple of the fundamental axial mode ( $f_8/f_1 = 7.3$  and  $f_9/f_1 = 7.78$ ). Additional informations are given by figure (18) which presents the acoustic mode shapes for the first 10 resonance frequencies. It clearly appears that the present methodology was able to capture a pure transverse mode i.e. mode number 8 in Fig. (18). The frequency of this mode is  $f_8=1731$  Hz which is close to the first pure transverse acoustic mode based on the nozzle height ( $f_{\text{exact}}^{1T} = 1700$  Hz). Furthermore a coupled axial-transverse mode i.e. mode number 9 in Fig. (18) is predicted at  $f_9=1845$  Hz. Other mode shapes ( $n = 1, \dots, 7, 10, 13, 14$ ) can be assimilated to pure longitudinal modes because their resonance frequencies are close to a multiple of the first axial mode.

## 6 Concluding remarks

The purpose of this study was to assess if a time-domain CFD code could be used to predict acoustic resonances. The methodology is based on a combination of the well-known MIMO vibration testing procedure and acoustic excitation using loudspeakers. The shakers are replaced by elastically-deforming vibrating membranes and the dynamics of the fluid/structure system is characterized by using a time-domain CFD code. The simulated acoustic field is monitored at a sufficient number of points to define the mode shapes. The flow excitation was provided by taking into account deforming wall of the geometry. It was found that both white noise and sine sweep excitations are able to predict the correct resonance frequencies and the corresponding pressure mode shapes.

The results indicate that it is possible to perform the acoustic mode identification with good accuracy from 0.1 kHz up to about 3.0 kHz. In the case of the Délyery nozzle, the sine sweep excitation mechanism allows the identifica-

tion of a relative high number of resonance modes such as transverse acoustic modes. It must be noted that this relatively global aeroacoustic characterization requires only one unsteady RANS computation over a total simulation time corresponding to 30 periods of the fundamental acoustic mode. A second advantage of the method is its ability to take into account mean flow velocities, turbulence effects and temperature variations in representative engineering geometries within the flow solver. Such variations can be significant in many engineering applications such as self-excited engine afterburners and rocket boosters.

## References

- [1] R. Brahim, R. Brahim, A. Ghafourian, Mode identification of high-amplitude pressure waves in liquid rocket engines, *Journal of Sound and Vibration* 229 (2000) 973–991.
- [2] Z.-S. Lium, C. Huang, W.-M. Qian, Z. Liu, L.-Y. Jiang, I. Campbell, I. Yimer, Self-excited combustion oscillations of a burner: Cause and remedy, 10th. Int. Congress on Sound and Vibration, stockholm [S], July 7-10 (2003).
- [3] K. Hourigan, M. Welsh, M. Thompson, A. Stokes, Aerodynamic sources of acoustic resonance in a duct with baffles, *Journal of Fluids and Structures* 4 (1990) 345–370.
- [4] M. Welsh, K. Hourigan, L. Welsh, R. Downie, M. Thompson, A. Stokes, Acoustics and experimental methods: The influence of sound on flow and heat transfer, *Experimental Thermal and Fluid Science* 3 (1990) 138–152.
- [5] J. French, Three-dimensional combustion stability modeling for solid rocket motors, *AIAA Paper* 98–3702 (1998).
- [6] S. Ziada, A. Oengoren, A. Vogel, Acoustics resonance in the inlet scroll of a turbo-compressor, *Journal of Fluids and Structures* 16 (2002) 361–373.
- [7] S. Pirozzoli, F. Grasso, Direct numerical simulation of impinging shock wave/turbulent boundary layer interaction at  $m=2.25$ , *Physics of Fluids* 18.
- [8] C. Loh, K. Zaman, Numerical investigation of "transonic resonance" with a convergent-divergent nozzle, *NASA/TM–2002-211324* (2002).
- [9] M. Debiasi, M. Samimy, Logic-based active control of subsonic cavity flow resonance, *AIAA Journal* 42 (2004) 1901–1909.
- [10] J. Anthoine, P. Planquart, D. Olivari, Cold flow investigation of the flow acoustic coupling in solid propellant boosters, *AIAA Paper* 98–0475 (1998).
- [11] J. Anthoine, D. Olivari, S. Hulshoff, M. V. Rooij, Qualitative model of vortex induced oscillations in a model of solid propellant boosters, *AIAA Paper* 98–2270 (1998).
- [12] J. Anthoine, J.-M. Buchlin, A. Hirschberh, Theoretical modelling of the effect of the nozzle cavity volume on the resonance level in large solid rocket motors, *AIAA Paper* 98–2102 (1998).
- [13] A. Stubos, C. Benocci, E. Palli, D. O. G.K. Stoubosxi and, Aerodynamically generated acoustic resonance in a pipe with annular flow restrictors, *Journal of Fluids and Structures* 13 (1999) 755–778.
- [14] H. Osman, M. Johnson, C. Fuller, P. Marcotte, Interior noise reduction of com-

posite cylinders using distributed vibration absorbers, AIAA Paper 2001–2230 (2001).

- [15] K. Holland, P. Davies, The measurement of sound power flux in flow ducts, *Journal of Sound and Vibration* 230 (2000) 915–932.
- [16] K. Holland, P. Davies, D. van der Walt, Sound power flux measurements in strongly excited ducts with flows, *Journal of Acoustical Society of America* 112 (2000) 2863–2871.
- [17] A. Sayma, M. Vahdati, L. Sbardella, M. Imregun, Modelling of 3d viscous compressible turbomachinery flows using unstructured hybrids grids, *AIAA Journal* 36 (2000) 945–954.
- [18] J. Détery, Experimental investigation of turbulence properties in transonic shock/boundary-layer interactions, *AIAA Journal* 21 (1983) 180–185.
- [19] J.-C. Chassaing, G. Gerolymos, I. Vallet, Reynolds-stress model dual-time-stepping computation of unsteady 3-d flows, *AIAA Journal* 41 (2003) 1882–1894.

## Appendix: Nomenclature

$a$	= sound velocity
$c$	= viscous damping
$E[\cdot]$	= expectation operator
$f_{\text{ex}}$	= excitation frequency
$f_n$	= undamped natural frequency
$G_{xx}$	= one-sided auto-spectrum density function ( $\in \mathbb{C}^{N_i \times N_i}$ )
$G_{xy}$	= one-sided cross-spectrum density function ( $\in \mathbb{C}^{N_i \times N_o}$ )
$H_{xy}$	= frequency response function ( $\in \mathbb{C}^{N_i \times N_o}$ )
$k$	= stiffness
$L$	= length
$m$	= mass
$n$	= mode number
$n_{\text{max}}$	= number of time steps
$N_i$	= number of inputs
$N_i$	= number of samples
$N_o$	= number of outputs
$R$	= radius
$S_{xy}$	= cross-spectrum density function ( $\in \mathbb{C}^{N_i \times N_o}$ )
$t$	= time
$t_{\text{max}}$	= total simulation time
$x(t)$	= input signal
$y(t)$	= output signal
$X(f)$	= forward Fourier transform of the input
$Y(f)$	= forward Fourier transform of the output
$\Delta f$	= frequency resolution
$\phi(f)$	= phase factor of $H_{xy}(f)$
$\partial S$	= surface of the vibrating wall

*Subscripts*

- $n$  = mode number
- $i$  = input
- $i, j, k$  = vector component along the corresponding direction
- $k$  = sample number
- $o$  = output

*Superscripts*

- $nA$  =  $n^{\text{th}}$  axial mode number
- $T$  = transpose
- $*$  = complex conjugate

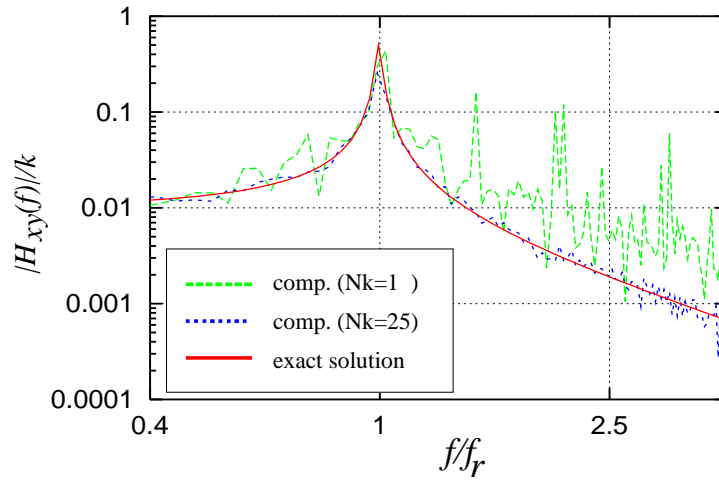


Fig. 1. Comparison of exact and computed gain factor of the frequency response function for the 1-DOF mechanical system

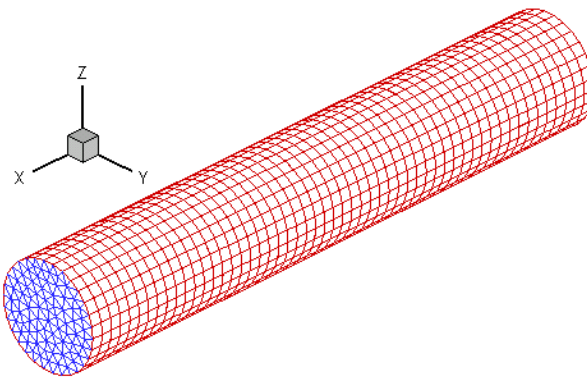


Fig. 2. Computational grid with 1736 nodes used for the zero-flow acoustic characterization of the circular cylinder configuration ( $L = 405.5$  mm,  $R = 38$  mm)

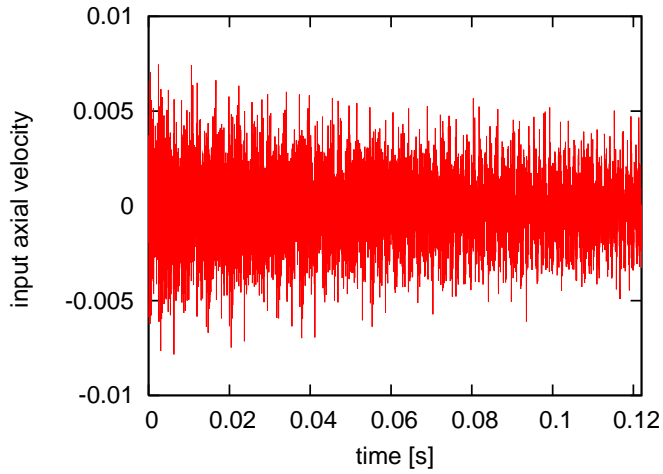


Fig. 3. Time-history of the axial velocity excitation imposed as input at the inflow ( $x/L = 0$ )

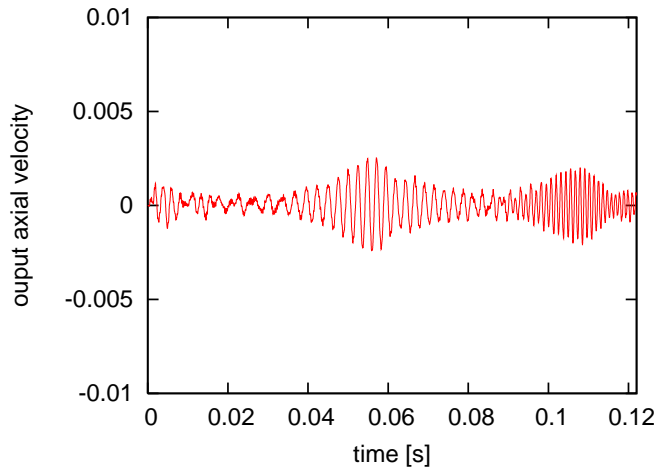


Fig. 4. Time-history of the axial velocity response taken at the middle axis of the duct ( $x/L = 0.5$ )

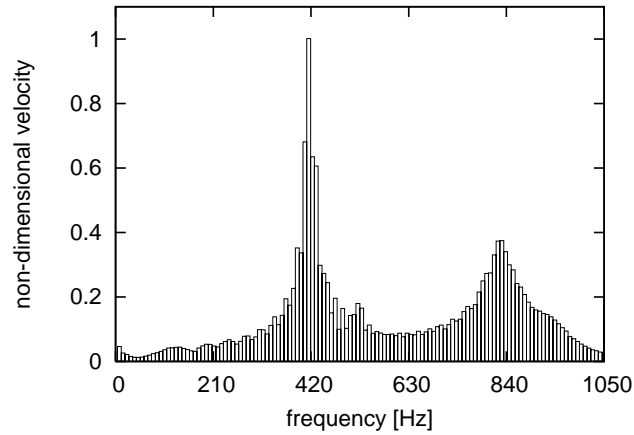


Fig. 5. Velocity spectrum using non-uniform time dependent random forcing (equations (6), (7)); the amplitude is dimensionless using the amplitude of the first axial mode; exact resonance frequencies are  $f_{\text{exact}}^{1A} = 423$  Hz and  $f_{\text{exact}}^{2A} = 846$  Hz)

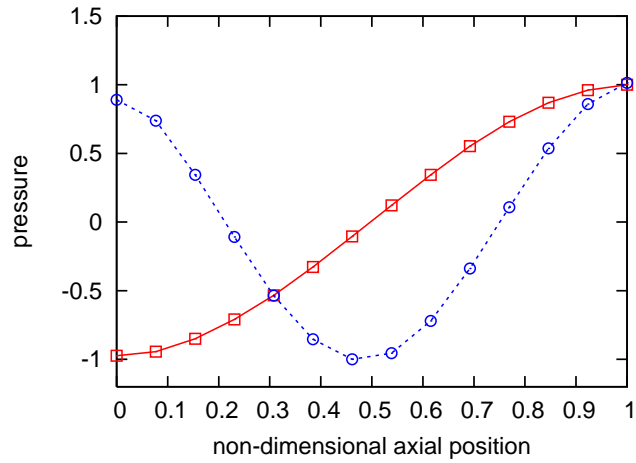


Fig. 6. Numerical prediction of the first two fundamental pressure mode shapes due to randomly vibrating wall for  $L = 405.5$  mm (— 1<sup>st</sup> axial mode ( $f^{1A} = 419$  Hz); - - - 2<sup>nd</sup> axial mode ( $f^{2A} = 838$  Hz))

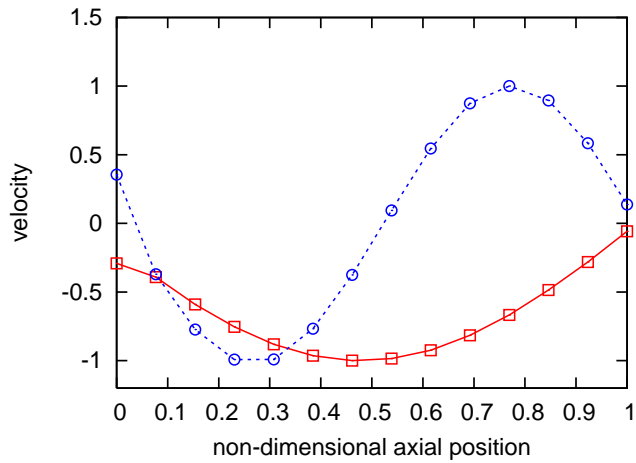


Fig. 7. First two fundamental velocity mode shapes due to randomly vibrating wall (— 1<sup>st</sup> axial mode ( $f^{1A} = 419$  Hz); - - - 2<sup>nd</sup> axial mode ( $f^{2A} = 838$  Hz));  $L = 405.5$  mm

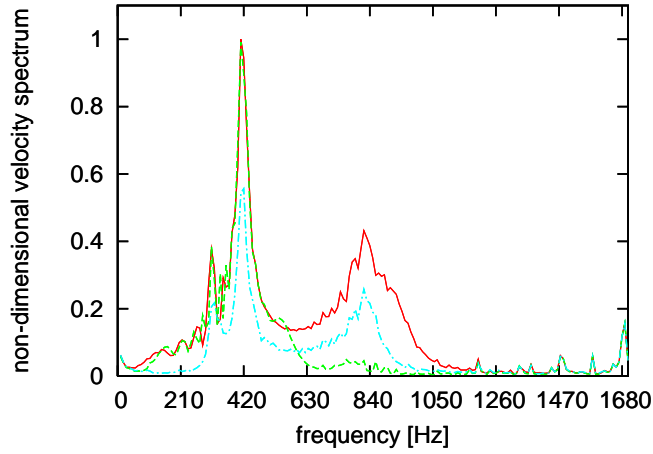


Fig. 8. Influence of the excitation frequency window for the configuration  $L = 405.5$  mm ( — case (a): [50 Hz; 999 Hz]; - - - case (b): [100 Hz; 600 Hz]; - · - case (c): [300 Hz; 900 Hz];  $f_{\text{exact}}^{1A} = 423$  Hz,  $f_{\text{exact}}^{2A} = 846$  Hz )

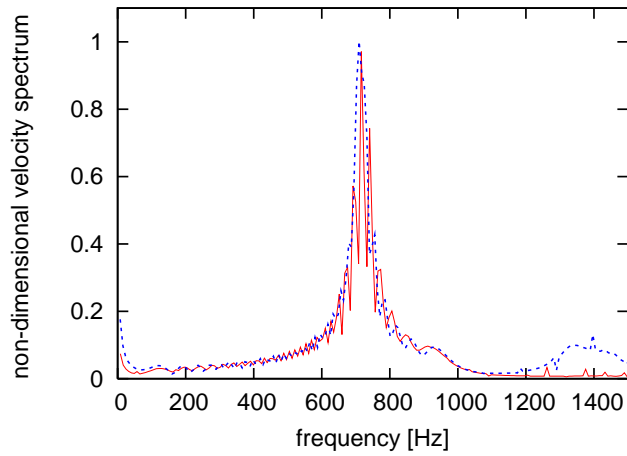


Fig. 9. Effect of the time-step for the configuration  $L = 231$  mm ( —  $\Delta t = 1.5 \times 10^{-5}$  s; - - -  $\Delta t = 0.8 \times 10^{-5}$  s;  $f_{\text{exact}}^{1A} = 742$  Hz )

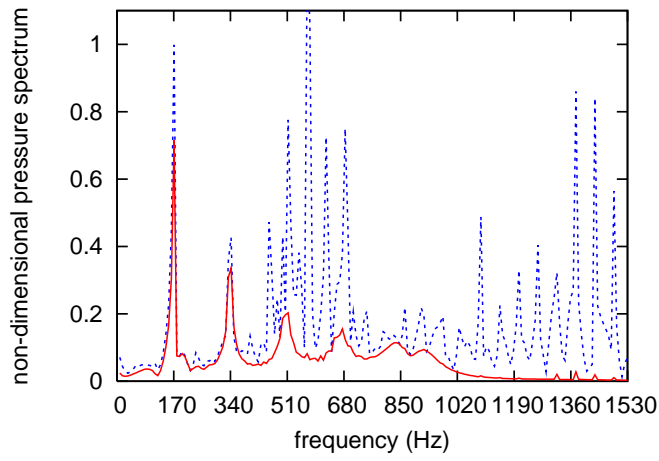


Fig. 10. Comparison of the velocity spectrum amplitude resulting from different random excitation mechanisms (— deforming piston excitations; - - - solid piston excitations;  $L = 1$  m,  $f_{\text{exact}}^{1A} = 170$  Hz,  $f_{\text{exact}}^{2A} = 340$  Hz,  $f_{\text{exact}}^{3A} = 510$  Hz)

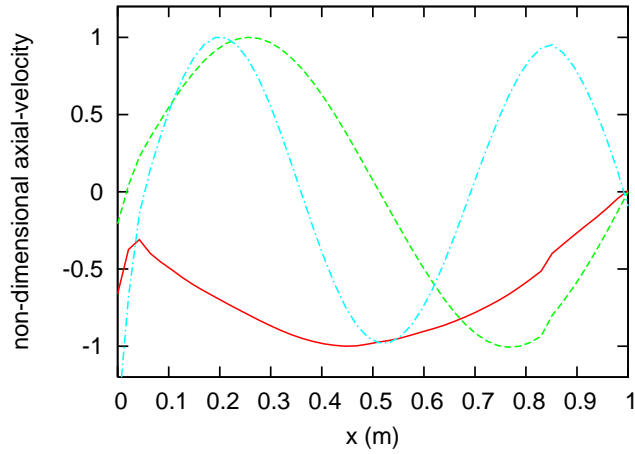


Fig. 11. First three velocity mode shape in a closed cylinder of length  $L = 1$  m resulting from a random deformation of the wall (— 1<sup>st</sup> mode ( $f^{1A} = 170$  Hz); - - - 2<sup>nd</sup> mode ( $f^{2A} = 340$  Hz); - - - 3<sup>rd</sup> axial mode at  $f^{3A} = 510$  Hz)

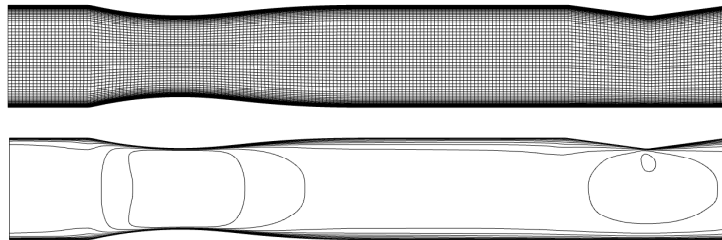


Fig. 12. Computational grid of the Délely B nozzle ( $N_i \times N_j = 201 \times 101$ ) and steady Mach number for an inlet flow velocity  $u_0 = 17\text{ms}^{-1}$

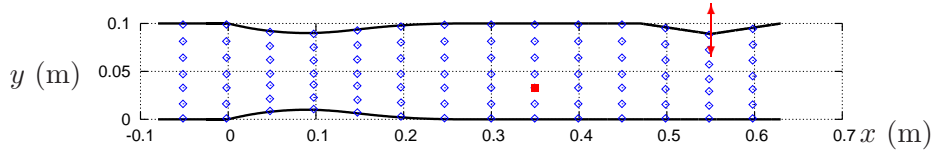


Fig. 13. Position of the "pressure sensors" (square symbol indicates the location of the reference sensor:  $x = 350$  mm,  $y = 30$  mm used to analyse the pressure spectra)

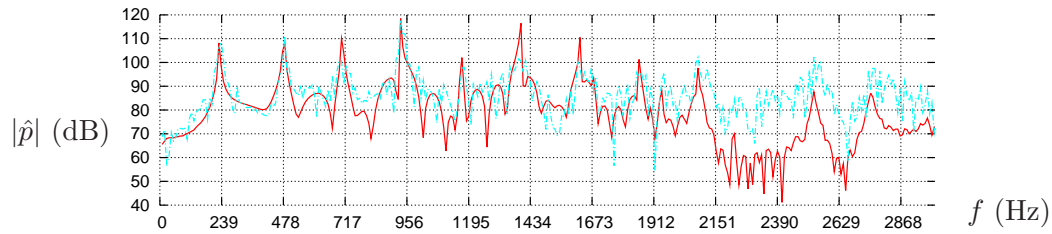


Fig. 14. Influence of the unsteady flow response due to random excitation and sine sweep excitation on the pressure spectrum amplitude (— sine sweep excitation; - - - random excitation)

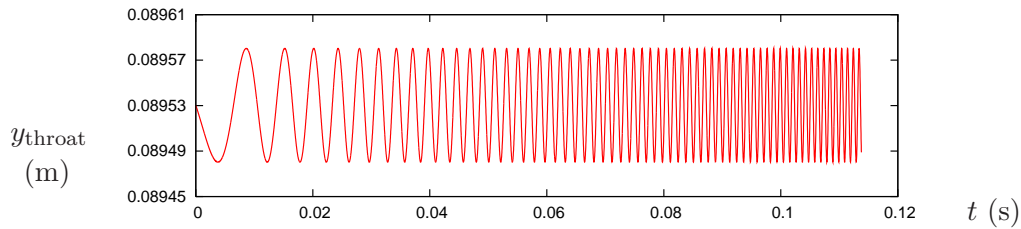


Fig. 15. Vertical displacement of the 2nd throat due to sine-sweep excitations for the 100 Hz - 3000 Hz range

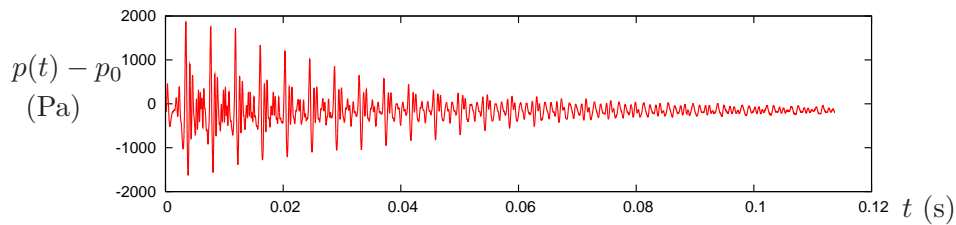


Fig. 16. Time history of the pressure fluctuation extracted at point  $x = 350$  mm and  $y = 30$  mm

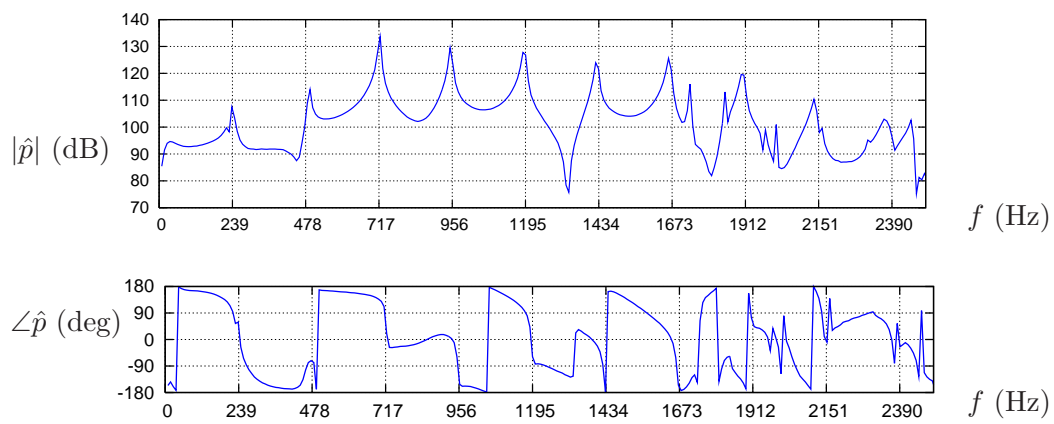


Fig. 17. Frequency response of the pressure signal at point  $x = 350$  mm and  $y = 30$ mm

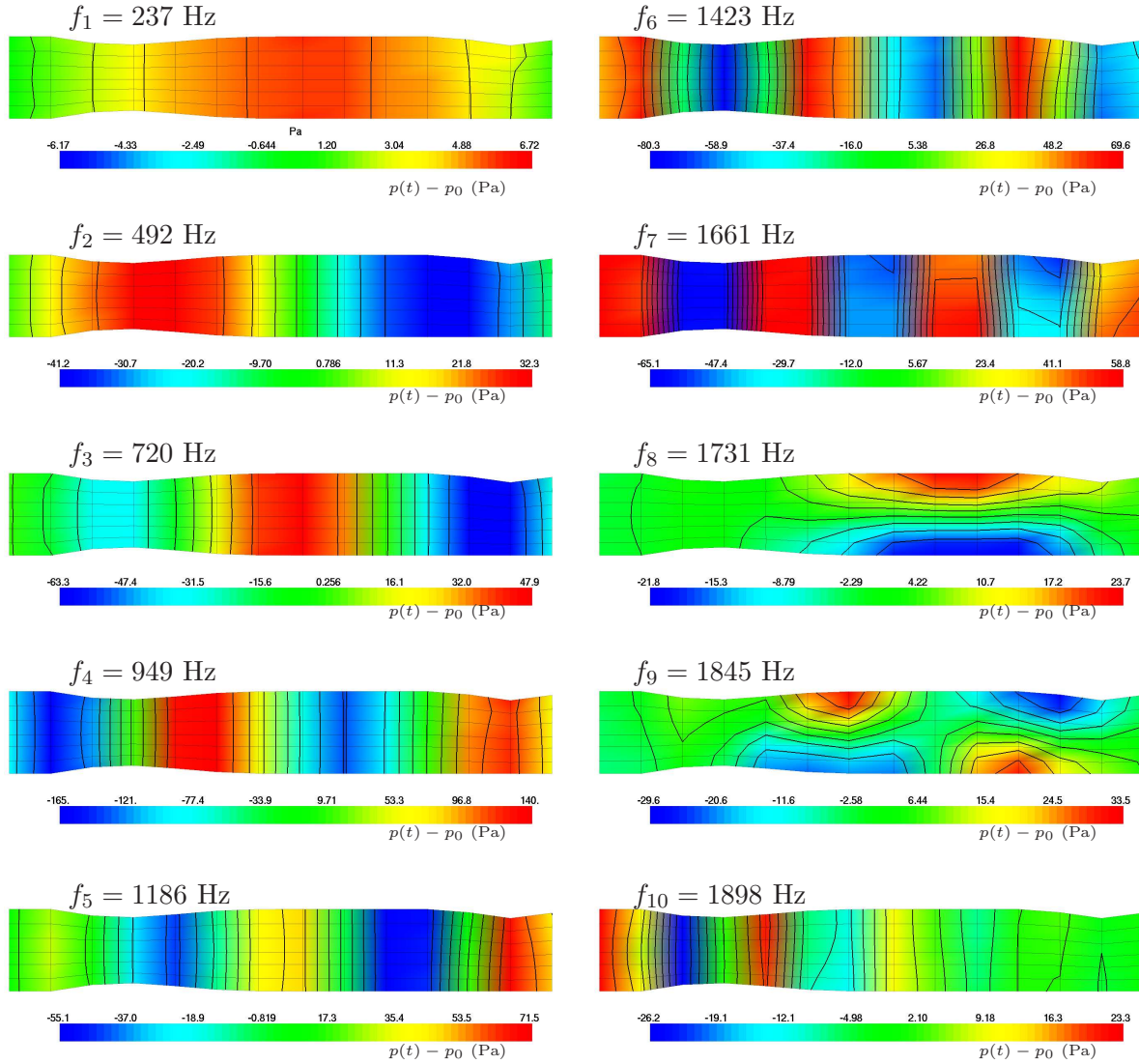


Fig. 18. Acoustic modes of the Déleré nozzle for an inlet flow velocity  $u_0 = 17 \text{ ms}^{-1}$  ( $\Delta t = 6.94 \times 10^{-6} \text{ s}$ ,  $T=0.113 \text{ s}$ ,  $\Delta f = 8 \text{ Hz}$ ,  $\Delta_h = 0.1 \text{ mm}$ )